Available online at www.sciencedirect.com
SCIENCE DIRECT®
International Journal of Multiphase Flow 32 (2006) 106–131
International Journal of Multiphase Flow
www.elsevier.com/locate/ijmulflow

Analysis of the flow in inhomogeneous particle beds using the spatially averaged two-fluid equations

Andreas ten Cate Sankaran Sundaresan *

Department of Chemical Engineering, School of Engineering and Applied Science, Princeton University, Princeton, NJ 08544, USA

Received 18 April 2005; received in revised form 15 August 2005

Abstract

The drag force term appearing in two-fluid models for fluid–particle flows is commonly closed by expressing it as a function of the local quantities, such as the local particle volume fraction, the local slip velocity between the particle and fluid phases, and the local mean-squared fluctuating velocity of the particles. The adequacy of such closures for inhomogeneous suspensions has been debated in the literature and some researchers have suggested the need for additional terms involving spatial gradients in these quantities. To test this proposition, simulations of flow in inhomogeneous steady beds of particles have been performed using the lattice-Boltzmann method. The particle beds consisted of disordered assemblies with a density profile on a scale much larger than the particle radius. Inhomogeneous beds with a controlled density profile were generated in three different ways, (i) by inhomogeneous stretching of the particle bed in one direction, (ii) by applying an inhomogeneous force to the particle phase during random motion of the particles, and (iii) by taking snapshots of a direct simulation of a traveling wave in a fluidization simulation. The global structure of the three beds was comparable, while assessment of the radial distribution functions showed that the three beds exhibited clearly different microscopic structures.

The force profiles along the inhomogeneous direction of the particle bed were obtained from the flow simulations. These were analyzed by applying spatial averaging in a manner identical to the averaging procedure that is used to derive the two-fluid model equations. The force profiles were compared to predictions based on flow simulations of homogeneous disordered particle beds over a range of volume fractions. To assess the role of the microstructure of the particle bed also simulations were executed where the homogeneous disordered bed was modified by either applying homogeneous stretching or by applying a lubrication force during generation of the particle bed.

This study demonstrated that the microscopic structure of the particle bed has a severe impact on the closure of the drag force. Our computations did not reveal any evidence supporting the need for terms involving gradients in particle volume fraction in the drag force closure.

Keywords: Lattice-Boltzmann; Drag force; Suspension; Closure

* Tel.: +1 609 258 4583; fax: +1 609 258 0211.
E-mail address: sundar@princeton.edu

0301-9322/$ - see front matter © 2005 Elsevier Ltd. All rights reserved.
doi:10.1016/j.ijmultiphaseflow.2005.08.001

1. Introduction

Fluid–particle systems such as fluidized beds manifest structures over a wide range of spatial and time scales. Experiments have revealed traveling voidage waves in liquid fluidized beds (Anderson and Jackson, 1968; Duru et al., 2002), bubble-like voids in beds fluidized by liquids (Duru et al., 2002) and gases (Rowe, 1964), and particle clusters in dilute fluidized beds. The origin of these structures has been the subject of many theoretical studies and numerical simulations, which have been reviewed by Jackson (2000). It is now known that averaged equations of motion (commonly referred to as the two-fluid model equations), obtained by ensemble or volume averaging the Navier–Stokes equations for the fluid and the Newton's equations for the motion of individual particles, coupled with very simple phenomenological closures for the effective stresses and the interphase interaction force appearing in them, can yield such structures in a qualitatively correct manner (Glasser et al., 1996, 1997; Jackson, 2000; Sundaresan, 2003). An important challenge ahead of us is the construction of more accurate and validated closures for the two-fluid model that can lead to quantitative predictions.

In most fluidized suspension flow problems and flows through fixed beds encountered in practice, the dominant terms appearing on the right hand side of the momentum balance equations are the body force term, the term accounting for the effect of the locally averaged pressure gradient in the continuous fluid phase, and the interphase interaction force term; there is little difficulty in describing the first of these terms, and the pressure gradient is computed as a part of the solution, when the two phases are incompressible. The interphase interaction term requires closure modeling, and the quantitative predictions of the two-fluid model depend strongly on the accuracy of the closure modeling of this term. The interphase interaction force is usually written as a sum of different contributions: the quasi-steady drag force, the added mass force, Basset history force, the inertial lift force, the Saffman lift force, etc. In most practical situations, the largest contribution to the interphase interaction force comes from the drag force, and hence the focus tends to be on improved closures for the drag force term.

It is commonly assumed that the local-average drag force in fluid–particle systems can be quantified purely in terms of local quantities, i.e., the local particle volume fraction (or equivalently voidage), the local average velocities of the fluid and particle phases, local mean-squared fluctuation velocity of the particles, and the fluid properties (e.g. Wylie et al., 2003). Spatial gradients in these quantities are generally not accounted for in the closure for the drag force. It was suggested by Foscolo and Gibilaro (1984) that the drag force should include a term proportional to the gradient in particle volume fraction and that this term plays an important role in the stabilization of some homogeneously fluidized states; this has been received with some skepticism in the literature (Batchelor, 1988).

More recently, Marchioro et al. (2000, 2001) have analyzed slow viscous flow of a fluid in domains with a small spatial gradient in particle volume fraction and explored the effects of these gradients on terms arising in two-fluid model equations. Wang and Prosperetti (2001) applied this approach to study slow viscous flows in fixed beds of stationary or spinning particles, allowing for a small-amplitude, sinusoidal variation of the particle volume fraction and found that the commonly used closure relations for the interphase interaction force, which are based on particle volume fraction, velocities and the pressure, are, in general, insufficient.

In the present study, we focus on fluid flow through assemblies of uniformly sized spherical particles and address the following two questions:

- Is it adequate to model the drag force on the basis of local quantities alone, without bringing in explicitly a dependence on gradients in particle volume fraction?
- Drag force models for fluid flow through random assemblies of particles typically consider the particle size and particle volume fraction as parameters characterizing the bed. However, macroscopically similar (and disordered) particle assemblies can have different microstructural details (such as the radial distribution function). How important are these details for the drag force between the fluid and particle phases?

To address these questions, we have performed detailed simulations of fluid flow in fixed beds of uniformly sized spherical particles in a variety of configurations. Simulations have been performed in homogeneous fixed

beds with randomized particle configurations created via different schemes to obtain different microstructural details, and in inhomogeneous beds of randomized particle configurations created in three different ways. All the simulations were performed in fixed beds of particles in periodic domains, with the inhomogeneity (in a statistical sense) limited to one of the principal directions of the domain, which also was the streamwise direction for the fluid flow.

For the direct simulations presented in this paper, the lattice-Boltzmann method is used. This method has been used by a number of authors to study the closure of drag forces in homogeneous ensembles of spheres (e.g. Kandhai et al., 2003; Hill et al., 2001a). The lattice-Boltzmann method is an efficient numerical scheme for simulation of fluid flow that performs very well on parallel computer platforms (Rothman and Zaleski, 1997; Chopard and Droz, 1998; Succi, 2001; Chen and Doolen, 1998). The application of this method to direct simulation of particle suspensions has been first proposed and established by Ladd (1994a).

From our detailed simulation results, we obtained locally averaged quantities, using the same definitions that went into the averaging of the Navier–Stokes equations for the fluid and the Newton's equations for the particles. This allowed us to directly compute all the terms appearing in the averaged equations for the fluid phase, and probe the effect of filter length on them.

Using results obtained from homogeneous and inhomogeneous beds created via different schemes, we will demonstrate that the microstructural details (specifically, the magnitude of the radial distribution function near contact and the presence of an anisotropy in the radial distribution function) can have appreciable quantitative effects on the drag force between the particles and the fluid. Our simulations did not reveal the need for terms involving gradients in particle volume fraction in the closure for the drag force.

The paper is organized as follows. The two-fluid model equations are presented and discussed in Section 2. The lattice-Boltzmann (LB) scheme used to simulate fluid flow through packed beds is then outlined in Section 3. Spatial filtering of all quantities obtained from the inhomogeneous geometries is presented in Section 4. Section 5 is devoted to spatial averaging of the results generated through the LB simulations to deduce spatial variation of the various terms in the two-fluid model equations. The variation of the hydrodynamic force along inhomogeneous particle beds is discussed in Section 6, bringing out the role of the microstructure. Section 7 summarizes the main findings of this study.

2. The two-fluid description of flow in a steady particle bed

Equations of motion for the fluid and particle phases, with locally averaged quantities such as particle volume fraction and the phase velocities as the dependent variables, can readily be obtained from the Navier–Stokes equations for the fluid phase and Newton's equations applied to the individual particles. Such equations, frequently referred to as the two-fluid model equations, have been derived in the literature through ensemble-averaging (e.g., see Zhang and Prosperetti, 1994; Marchioro et al., 2001) and volume-averaging (e.g., see Jackson, 2000) procedures, both of which have been shown to yield the same result (Jackson, 2000, 1997). In the present manuscript, we apply a combination of ensemble and spatial averaging to extract locally averaged quantities from detailed flow simulations. Such mixed averaging does not affect the form of the two-fluid model equations, but allows us to extract locally averaged quantities from fewer detailed simulations. The details of the averaging procedure can be found in the literature, and it suffices to say here that the two-fluid model consists of two continuity equations,

$$\frac{\partial \rho_s \phi}{\partial t} + \nabla \cdot (\rho_s \phi \mathbf{u}_s) = 0, \tag{1}$$

$$\frac{\partial \rho_f (1-\phi)}{\partial t} + \nabla \cdot (\rho_f (1-\phi) \mathbf{u}_f) = 0, \tag{2}$$

and two momentum balances,

$$\rho_s \phi \left[\frac{\partial \mathbf{u}_s}{\partial t} + \mathbf{u}_s \cdot \nabla \mathbf{u}_s \right] = \phi \nabla \cdot \boldsymbol{\Pi}_f + \nabla \cdot \boldsymbol{\Pi}_s + \mathbf{f} + \phi \rho_s \mathbf{g}, \tag{3}$$

$$\rho_f (1-\phi) \left[\frac{\partial \mathbf{u}_f}{\partial t} + \mathbf{u}_f \cdot \nabla \mathbf{u}_f \right] = (1-\phi) \nabla \cdot \boldsymbol{\Pi}_f - \nabla \cdot \boldsymbol{\Pi}'_f + \mathbf{T} - \mathbf{f} + (1-\phi) \rho_f \mathbf{g}, \tag{4}$$

for the solid phase and fluid phase, respectively. Here, ρ_s and ρ_f are the densities of the particles and the fluid, $\mathbf{u}_s$ and $\mathbf{u}_f$ are the local-average particle and fluid phase velocities, and ϕ is the volume fraction of the particle phase. The hydrodynamic interaction force between the particle and the fluid phase is given by $\mathbf{f}$. The body force acceleration is indicated by $\mathbf{g}$. $\mathbf{\Pi}_s$ and $\mathbf{\Pi}_f$ are the effective particle and fluid phase stress tensors, $\mathbf{\Pi}'_f$ is a stress associated with fluctuations in fluid velocity and $\mathbf{T}$ is the divergence of a fluid–particle stress term (described later). As we restrict our attention to steady flow of fluid through a fixed bed of particles, the unsteady terms in (1)–(4) can be set to zero.

The spatial averaging procedure through which these equations were obtained is based on a normalized spatial averaging function g, centered at location $\mathbf{x}$,

$$\int_V g(|\mathbf{x}-\mathbf{y}|)\,\mathrm{d}V_y = 1. \tag{5}$$

The local volume fraction for the fluid phase is determined as

$$(1-\phi)(\mathbf{x}) = \left\langle \int_{V_f} g(|\mathbf{x}-\mathbf{y}|)\,\mathrm{d}V_y \right\rangle, \tag{6}$$

where V_f indicates that the integral is taken over that part of the domain that is occupied by the fluid and the angle brackets indicate averaging over many realizations. The local-average fluid velocity is determined as

$$\mathbf{u}_f(\mathbf{x}) = \frac{1}{(1-\phi)} \left\langle \int_{V_f} \mathbf{u}(\mathbf{y}) g(|\mathbf{x}-\mathbf{y}|)\,\mathrm{d}V_y \right\rangle. \tag{7}$$

This velocity will be designated the interstitial velocity. The superficial velocity $\bar{\mathbf{u}}_f$, is given by $\bar{\mathbf{u}}_f = \mathbf{u}_f(1-\phi)$.

In this paper we follow Jackson (1997) and define the averaged quantities for the solid phase as particle-phase averages. This means that all properties of a particle, such as the net velocity, force, torque, etc., are calculated for each particle by integration over the particle surface and are assigned to the center of the particle. In this manner, the local-average particle number density $n(\mathbf{x})$ is computed from the location of the center of mass of the particle, $\mathbf{x}_p$, as

$$n(\mathbf{x}) = \left\langle \sum_p g(|\mathbf{x}-\mathbf{x}_p|) \right\rangle, \tag{8}$$

from which the solid phase volume fraction in first order approximation is determined as $\phi(\mathbf{x}) = n(\mathbf{x})v_p$, where v_p is the particle volume. The objective of the present study is to analyze the flow field in fixed beds of spherical particles with a spatial variation of the particle number density only in the mean flow direction (henceforth denoted by x), i.e. $n(\mathbf{x})$ is only a function of x. In the presence of such a spatial gradient in the particle number density, a more accurate relationship between $\phi(x)$ and $n(x)$ is given by

$$\phi(x) = \frac{4}{3}\pi a^3 n(x) + \frac{2}{15}\pi a^5 \frac{\mathrm{d}^2 n(x)}{\mathrm{d}x^2} + \text{h.o.t.}, \tag{9}$$

where a denotes the particle radius. However, in all the cases examined here, all the terms on the right hand side of this equation except the first one are negligible and hence the lowest order approximation is adequate.

In our simulations we have considered many realizations of particle configurations which, in a statistical sense, were consistent with a stipulated gradient in the particle number density. For each realization, a body force was applied in the x-direction (only) to the fluid phase, and the resulting steady fluid flow field was computed. As one can expect, in such simulations, the local average fluid velocity is non-zero only in the x-direction, and when the fluid is incompressible, the local average superficial velocity is independent of position.

The particle phase averaged velocity is given by

$$\mathbf{u}_s(\mathbf{x}) = \frac{1}{n} \left\langle \sum_p \mathbf{u}_p g(|\mathbf{x}-\mathbf{x}_p|) \right\rangle. \tag{10}$$

As we are concerned with fixed beds of particles, $\mathbf{u}_p$ is zero for every particle and hence $\mathbf{u}_s$ is identically zero. In this case, the particle phase continuity and momentum balance equations are not required for our analysis. We

can, however, observe that the total hydrodynamic force per unit volume of the fixed bed **F**, exerted on the particles by the fluid, is given by

$$\mathbf{F} = \left\langle \sum_{\mathrm{p}} g(|\mathbf{x}-\mathbf{x}_{\mathrm{p}}|) \int_{s_{\mathrm{p}}} \mathbf{n}\cdot\boldsymbol{\sigma}(\mathbf{y})\,\mathrm{d}S_y \right\rangle = \phi\nabla\cdot\boldsymbol{\Pi}_{\mathrm{f}} + \mathbf{f}, \tag{11}$$

where s_{p} denotes the surface of the pth particle and **n** is the unit outward normal on the particle surface (pointing into the fluid). $\boldsymbol{\Pi}_{\mathrm{f}}(\mathbf{x})$ is the effective fluid phase stress tensor at the location **x**, and is given by

$$\boldsymbol{\Pi}_{\mathrm{f}} = \frac{1}{(1-\phi)} \left\langle \int_{V_{\mathrm{f}}} \boldsymbol{\sigma}(\mathbf{y}) g(|\mathbf{x}-\mathbf{y}|)\,\mathrm{d}V_y \right\rangle, \tag{12}$$

where $\boldsymbol{\sigma}$ denotes the fluid phase stress tensor obtained from the detailed fluid flow field in the interstices between the particles. For a Newtonian fluid,

$$\boldsymbol{\sigma} = -p\mathbf{I} + \mu((\nabla u) + (\nabla u)^{\mathrm{T}}). \tag{13}$$

It can be shown that for the one-dimensional flow studied here, the deviatoric terms in (13) do not contribute to (12), so that

$$\boldsymbol{\Pi}_{\mathrm{f}} = -p_{\mathrm{f}}(\mathbf{x})\mathbf{I}; \quad p_{\mathrm{f}}(\mathbf{x}) = \frac{1}{(1-\phi)} \left\langle \int_{V_{\mathrm{f}}} p(\mathbf{y}) g(|\mathbf{x}-\mathbf{y}|)\,\mathrm{d}V_y \right\rangle. \tag{14}$$

The stress tensor associated with fluid velocity fluctuations is given by

$$\boldsymbol{\Pi}'_{\mathrm{f}} = \left\langle \int_{V_{\mathrm{f}}} \rho(\mathbf{u}(\mathbf{y}) - \mathbf{u}_{\mathrm{f}}(\mathbf{y}))(\mathbf{u}(\mathbf{y}) - \mathbf{u}_{\mathrm{f}}(\mathbf{y})) g(|\mathbf{x}-\mathbf{y}|)\,\mathrm{d}V_y \right\rangle. \tag{15}$$

For the one-dimensional flow studied here, $\boldsymbol{\Pi}'_{\mathrm{f}}$ is diagonal and can be directly computed from the detailed simulations.

The force **T** (per unit bed volume) appearing in (4) arises because of the finite size of the particles (Jackson, 2000, 1997). The total fluid–particle interaction force appears in the particle-phase average as $\langle \sum_{\mathrm{p}} g(|\mathbf{x}-\mathbf{x}_{\mathrm{p}}|) \int_{s_{\mathrm{p}}} \mathbf{n}\cdot\boldsymbol{\sigma}(\mathbf{y})\,\mathrm{d}S_y \rangle$, while in the fluid phase equation it is given by $\langle \sum_{\mathrm{p}} \int_{s_{\mathrm{p}}} \mathbf{n}\cdot\boldsymbol{\sigma}(\mathbf{y}) g(|\mathbf{x}-\mathbf{y}|)\,\mathrm{d}S_y \rangle$, The difference between these two is captured by **T**. An expression for **T** can be deduced (Jackson, 2000, 1997) through a Taylor series expansion of $g(|\mathbf{x}-\mathbf{y}|)$ about $(\mathbf{x}-\mathbf{x}_{\mathrm{p}})$, and some algebraic manipulations:

$$\mathbf{T} = \nabla\cdot\mathbf{t}_1(\mathbf{x}) - \frac{1}{2}\nabla\nabla : \mathbf{t}_2(\mathbf{x}) + \text{h.o.t.}, \tag{16}$$

where the tensors $\mathbf{t}_i$ are tensors of increasing order of the traction exerted on the surface of the sphere. These are given by

$$\mathbf{t}_1(\mathbf{x}) = a\left\langle \sum_{\mathrm{p}} g(|\mathbf{x}-\mathbf{x}_{\mathrm{p}}|) \int_{s_{\mathrm{p}}} \mathbf{n}\mathbf{n}\cdot(\boldsymbol{\sigma}(\mathbf{y}) - \boldsymbol{\Pi}_{\mathrm{f}}(\mathbf{y}))\,\mathrm{d}S_y \right\rangle, \tag{17}$$

$$\mathbf{t}_2(\mathbf{x}) = a^2\left\langle \sum_{\mathrm{p}} g(|\mathbf{x}-\mathbf{x}_{\mathrm{p}}|) \int_{s_{\mathrm{p}}} \mathbf{n}\mathbf{n}\mathbf{n}\cdot(\boldsymbol{\sigma}(\mathbf{y}) - \boldsymbol{\Pi}_{\mathrm{f}}(\mathbf{y}))\,\mathrm{d}S_y \right\rangle. \tag{18}$$

From the detailed solution of the Navier–Stokes equations describing fluid flow in inhomogeneous fixed beds, and the formal definition of each term presented above, we have performed a term-by-term analysis of all the terms appearing the two-fluid model. This is described in the following sections.

3. Direct simulation with the lattice-Boltzmann method

Direct simulation of the fluid motion around monodisperse spheres forms the basis for the analysis that we present in this paper. For direct simulation the lattice-Boltzmann method is used. The lattice-Boltzmann method provides an efficient numerical scheme to obtain an approximate solution for the Navier–Stokes equations in the low Mach number limit. The underlying principle is that the fluid is mimicked by a distribution of mass

that propagates on a cubic grid at discrete timesteps. The local distribution of the mass gives properties such as the local density, momentum, pressure and viscous stresses. The main features of the method are (i) that it is numerically stable over a wide range of flow conditions, (ii) that it handles complex geometries such as large clusters of particles without a need for additional computational complexities such as generation of unstructured meshes or local grid refinement, and (iii) that it scales excellently on distributed parallel computer platforms, since all computational operations are completely local. For recent literature on the method and applications we refer to Rothman and Zaleski (1997), Chopard and Droz (1998), Succi (2001), Chen and Doolen (1998) and Dazhi et al. (2003). The specific lattice-Boltzmann scheme used in this work is given by Eggels and Somers (1995).

The lattice-Boltzmann method has been used for direct simulations of particle suspensions by a number of authors. Suspension simulations have initially been established by Ladd (1994a,b), who mainly focussed on the dynamic properties of large ensembles of particles (see e.g. Ladd, 1997, 2002; Ladd and Verberg, 2001). The method has been recently used by Hill et al. (2001a,b) to analyze the fluid–particle interaction force in homogeneous fixed beds of uniformly sized particles. These authors have performed simulations over a range of Reynolds numbers, particle volume fractions and for different geometries (simple cubic, face centered cubic and random particle configurations in a large periodic box).

All the simulations described in this paper have been performed in periodic domains. The periodic domain was discretized using grids which are equally spaced in all three directions. In what follows, nodes refer to the points formed by the intersection of this grid network. In the lattice-Boltzmann method the units of all properties are expressed in terms of the discrete grid spacing Δx and the discrete time step Δt, which are both taken as unity, while mass is expressed in terms of the fluid density ρ, which was also set to unity in our simulations. Given that the lattice units $\Delta x = 1$ and $\Delta t = 1$ and all flow properties are generally presented in dimensionless form, no further explicit reference to units will be made throughout this paper.

Spheres were placed on the grid network by locating their centers at the desired locations (described later), without constraining the centers to lie exactly on the grid nodes themselves. The radius of the spheres as multiples of the grid spacing (henceforth referred to as particle input radius, a_0) was an input and using this information, all the nodes lying inside the particles were readily identified. A specific body force was applied to the fluid nodes (i.e. those lying outside the particles) and this drove the fluid flow through the bed. In all our simulations this body force was aligned with one of the principal directions of the periodic domain.

The no-slip boundary condition at the surface of the particles was imposed in the lattice-Boltzmann scheme via a regular bounce-back method (Ladd, 1994a). With this method, mass that is about to propagate into a solid object is reflected back into the fluid. The location of the bounce back node was assumed to be halfway between the fluid nodes and the node covered by the solid object. A schematic representation is given in Fig. 1 (note that mass propagates along the principle axes as well as diagonally across the grid). The total force on a particle was computed as

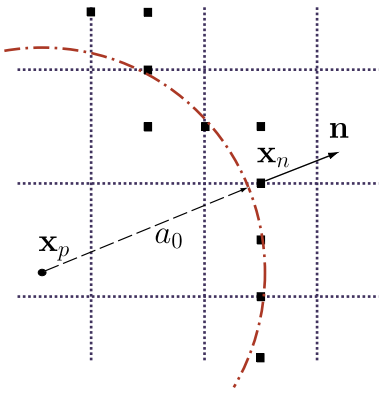

Fig. 1. Impression of the location of bounce back nodes (■) around a sphere surface of radius a. The gridnodes of the lattice-Boltzmann scheme are located at the intersection of the grid lines (dotted lines). The location of the sphere center is indicated by $\mathbf{x}_p$ and of the bounce back node as $\mathbf{x}_n$. The outward unit normal vector $\mathbf{n}$ is located at the bounce back node position.

$$\mathbf{F} = \sum_{N_\mathrm{p}} (\Delta\rho_i \mathbf{c}_i) \tag{19}$$

and is identical to the sum of the momentum change at the bounce-back nodes, where mass ρ_i, propagating in direction i at discrete grid velocity $\mathbf{c}_i$ reverses direction. The summation is taken over all boundary nodes N_p. The bounceback method was extended in the simulations such that the tensors $\mathbf{t}$ that appear in the spatially averaged vector $\mathbf{T}$ of (16) could be computed. For this purpose the surface integrals of (17) and (18) were approximated by

$$\mathbf{t}_1(\mathbf{x}) = a\left\langle \sum_\mathrm{p} g(|\mathbf{x}-\mathbf{x}_\mathrm{p}|)\left(\mathbf{s}_1(\mathbf{x}_\mathrm{p}) - \int_{s_\mathrm{p}} \mathbf{n}\mathbf{n}\cdot\boldsymbol{\Pi}_\mathrm{f}\,\mathrm{d}S_y\right)\right\rangle, \tag{20}$$

$$\mathbf{t}_2(\mathbf{x}) = a^2\left\langle \sum_\mathrm{p} g(|\mathbf{x}-\mathbf{x}_\mathrm{p}|)\left(\mathbf{s}_2(\mathbf{x}_\mathrm{p}) - \int_{s_\mathrm{p}} \mathbf{n}\mathbf{n}\mathbf{n}\cdot\boldsymbol{\Pi}_\mathrm{f}\,\mathrm{d}S_y\right)\right\rangle, \tag{21}$$

where the surface integral of the stress tensor at the particle surface, $\mathbf{s}_i$, is approximated as

$$\mathbf{s}_1(\mathbf{x}_\mathrm{p}) \simeq \sum_{N_\mathrm{p}} \mathbf{n}(\Delta\rho_i\mathbf{c}_i)(\mathbf{x}_n), \tag{22}$$

$$\mathbf{s}_2(\mathbf{x}_\mathrm{p}) \simeq \sum_{N_\mathrm{p}} \mathbf{n}\mathbf{n}(\Delta\rho_i\mathbf{c}_i)(\mathbf{x}_n), \tag{23}$$

where the outward normal $\mathbf{n}(\mathbf{x}_n)$ is computed at the location of the bounceback node, as indicated in Fig. 1.

As $\boldsymbol{\Pi}_\mathrm{f}$ is a smoothed variable, it is a continuous function, defined everywhere, including the region occupied by the particles. Through Taylor series expansion of $\boldsymbol{\Pi}_\mathrm{f}$ about the center of the spherical particles, followed by some algebraic manipulations, one can show that

$$a\left\langle \sum_\mathrm{p} g(|\mathbf{x}-\mathbf{x}_\mathrm{p}|)\int_{s_\mathrm{p}} \mathbf{n}\mathbf{n}\cdot\boldsymbol{\Pi}_\mathrm{f}\,\mathrm{d}S_y\right\rangle \simeq \phi\boldsymbol{\Pi}_\mathrm{f} \tag{24}$$

and

$$a^2\left\langle \sum_\mathrm{p} g(|\mathbf{x}-\mathbf{x}_\mathrm{p}|)\int_{s_\mathrm{p}} \mathbf{n}\mathbf{n}\mathbf{n}\cdot\boldsymbol{\Pi}_\mathrm{f}\,\mathrm{d}S_y\right\rangle \simeq 0 \tag{25}$$

by leading order.

The discrete cuts of the links halfway between the fluid nodes caused a sphere to become staircase shaped. As a result, for representation of a sphere on a cubic grid, a sufficiently high resolution is required. With this in mind, we have first tested the influence of the resolution of the simulations using various input radii. All simulations have been performed at a single kinematic viscosity of $\nu = 0.04$ in lattice units.

It is well known (e.g., see Hill et al., 2001a) that in simulation of flow in particle beds with the lattice-Boltzmann method, the effective or *hydrodynamic* radius of the particle is different from the input radius. The hydrodynamic radius a for a chosen input radius a_0, was determined through simulation of steady, low Reynolds number fluid flow through simple cubic arrays of stationary spheres, and by requiring the computed fluid–particle interaction force to agree with the results reported by Sangani and Acrivos (1982), e.g., see also Hill et al. (2001a). All simulations presented in this paper were performed at a single input radius $a_0 = 9.5$. The equivalent hydrodynamic radius was $a = 9.7$. All simulations were performed at a single particle Reynolds number $Re_\mathrm{p} = 2a\bar{u}_{x,\mathrm{f}}/\nu = 20$, with the mean flow aligned in the x-direction.

4. The quasi-1D particle bed

We have carried out many simulations of fluid flow in fixed beds with a spatial inhomogeneity in the streamwise direction. We now outline the filtering procedure used to obtain smoothly varying, locally-averaged quantities.

4.1. Filtering the periodic quasi-1D particle bed

Our intent was to perform simulations in fixed beds which are periodic in all three directions, statistically homogeneous in two of these three directions (y and z), and inhomogeneous in the streamwise direction (x). Therefore, the filtering was chosen to conform to this character. Specifically, the filter (weighting) function, $g(x)$, was chosen to be independent of y and z, and depend only on x. By definition, we must then have

$$\int_{L_y}\int_{L_z}\int_{x-\frac{1}{2}L_x}^{x+\frac{1}{2}L_x} g(\mathbf{x}-\xi)\,\mathrm{d}V_\xi = 1, \tag{26}$$

where L_y and L_z denote the homogeneous directions, and x is held constant during integration. We define a characteristic filter length ℓ according to

$$\int_{L_y}\int_{L_z}\int_{x-\ell}^{x+\ell} g(\mathbf{x}-\xi)\,\mathrm{d}V_\xi = \frac{1}{2}. \tag{27}$$

The filter function $g(x)$ is bounded in the x-direction and reaches zero at $x \pm L_\mathrm{f}$, the maximum distance around x at which filtering is performed. In the periodic domain the filtering range $[x - L_\mathrm{f}, x + L_\mathrm{f}]$ has to be chosen such that $L_\mathrm{f} \leqslant \frac{1}{2}L_x$ is obeyed.

The length scales of the simulation and averaging procedure are shown in Fig. 2, where the filter length is indicated for the specific case of a cosine shaped filter, given by

$$\begin{aligned} g(\mathbf{x}) &= \frac{1}{2L_\mathrm{f}L_yL_z}\left[1+\cos\left(\frac{\pi x}{L_\mathrm{f}}\right)\right] \quad \forall x - L_\mathrm{f} \leqslant x \leqslant x + L_\mathrm{f}, \\ g(\mathbf{x}) &= 0 \quad \forall x - \frac{1}{2}L_x < x < x - L_\mathrm{f}, \quad x + L_\mathrm{f} < x < x + \frac{1}{2}L_x. \end{aligned} \tag{28}$$

The action of this filter was tested on the analytic profile of the volume fraction of the stretched particle bed (see Section 4.2). In Fig. 3(a), it is demonstrated that when a filter with $\ell = 3a$ is applied, the profile gets smoothened and the peak and minimum of the profile shift towards the mean of the entire domain. For the present discussion, we can simply take the drawn line as an input function which, upon filtering, transforms to the dashed line with $\ell = 3a$ and dotted line when $\ell = 0.5a$. The extent of flattening seen in this figure increases with filter length ℓ, which is entirely obvious. The smaller filter length of $0.5a$ has the advantage of minimal flattening of the profile.

Since the two-fluid model presented earlier considers particle-phase averages, we assigned the volume of every particle in the fixed bed as a delta function located at the center of mass of that particle. The particle bed is then a sum of delta functions which, upon filtering, transforms to a continuous function. The continuous functions obtained in this manner for various realizations were then averaged to obtain the smoothed profile. Fig. 3(b) shows one such example. Fifty realizations of a homogeneous fixed bed were created and then stretched in one of the directions (see later for specific details) to induce inhomogeneous beds. (Because this stretching was a well-defined operation, the ensemble averaged volume fraction profile could be determined

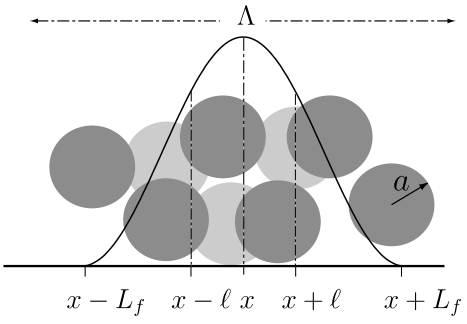

Fig. 2. Example of the length scales of spatial filtering of the particle field with a bounded cosine shaped filter.

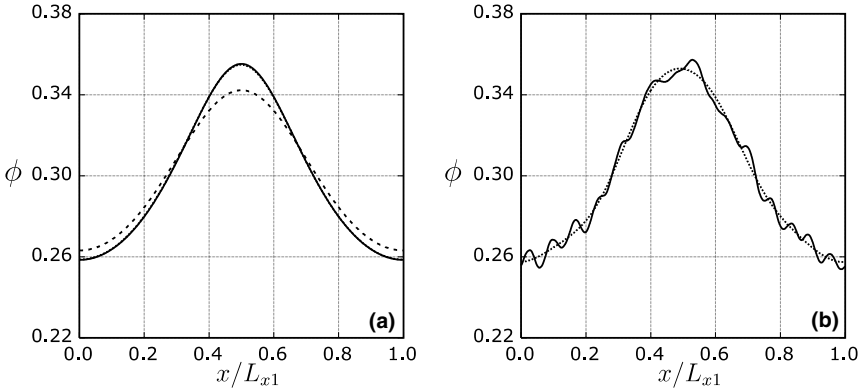

Fig. 3. Application of spatial averaging: (a) filtered analytical profile with $\ell = 3a$ (dashed line) and $\ell = 0.5a$ (dotted line) compared with the unfiltered analytic density profile (drawn line). The dotted and the drawn lines are essentially indistinguishable. (b) Application of a low pass filter (dotted line) on the density profile obtained by filtering and ensemble averaging of 50 particle beds (drawn line, $\ell = 0.5a$). L_{x1} is the box length in the x-direction.

analytically. The drawn line in Fig. 3(a) is indeed this analytical function.) The particle volume fraction distribution obtained by first filtering each realization with $\ell = 0.5a$ and then by averaging over the realizations is shown as the drawn line in this figure. The presence of small wiggles is clearly evident; although they could have been easily removed by increasing ℓ to $3.0a$, it would have resulted in a noticeable flattening of the curve. The dotted line in Fig. 3(b) was obtained by performing a Fourier transform of the drawn line and retaining only the low-order modes; specifically, the modes with wavenumber larger than $0.1(2\pi/a)$ were discarded. This approach produced smoothened results without flattening the primary peak and valley in the volume fraction profile.

4.2. The stretched RND particle bed (ST)

Random homogeneous particle beds were obtained by placing a number of particles in a fully periodic box and initializing the particles with a random velocity. Hard sphere collision detection was applied to keep the spheres separated (see Chen et al., 1998 for details). Random beds were obtained by selecting instantaneous snapshots of the developing particle field at large time intervals (typically 500.000 discrete time steps) to assure that the different geometries were uncorrelated. The spanwise box dimensions L_y and L_z were chosen as 10 particle radii, which was sufficiently large to assure that there was minimal impact of the periodicity of the box on the structure of the random particle bed. This will be demonstrated below.

Inhomogeneous stretching was applied to create a macroscopic density profile in a controlled manner. The particle bed is generated at an initial length L_{x0}. Then, the positions of the center of mass of the particles were shifted from x_0 to x_1 according to

$$x_1 = (1+\alpha)x_0 + \beta \sin\left(\frac{2\pi x_0}{L_{x0}}\right), \tag{29}$$

where α and β are parameters that determine the degree of stretching and the amplitude of the density profile, respectively. The new bed length is $L_{x1} = L_{x0}(1+\alpha)$. One restriction to the choice of the parameters α and β is that upon displacement one needs to prevent particles from overlapping. This can be ensured by demanding that

$$\frac{\mathrm{d}x_1}{\mathrm{d}x_0} > 1 \tag{30}$$

everywhere. The analytic density profile can be determined based on an initially uniform volume fraction ϕ_0 as

$$\phi(x_0) = \phi_0\left(1+\alpha+\frac{2\pi\beta}{L_{x0}}\cos\left(\frac{2\pi\beta x_0}{L_{x0}}\right)\right)^{-1}. \tag{31}$$

The initial volume fraction was $\phi_0 = 0.36$. This volume fraction was chosen to stay well away from the regime in which thermalized hard sphere ensembles may crystallize (i.e. for $\phi > 0.5$, Hill et al., 2001b). The initial box length L_{x0} was $36.3a$ and contained 310 spheres. The stretching parameters were chosen as $\alpha = 0.2$ and $\beta = 14$ which was just above the limit of Eq. (30). The mean volume fraction of the stretched particle bed became $\phi_m = 0.3$. Since each system only contained 310 spheres, 50 particle beds were used for simulation of the stretched particle beds so that ensemble averaging could be used to obtain smooth results. The volume profile of the ensemble average of the stretched beds (henceforth called ST) is plotted in Fig. 4 and compared with the analytical profile.

In Fig. 4(a) and (b) the effect of increasing the filter length from $0.5a$ to $3a$ is shown and compared to the filtered analytical profile of the ST particle bed. The figure shows that at both instances, the filtered profile follows the filtered analytical profile accurately. At the smallest filter length a small deviation from the filtered analytical profile is observed but generally the profile is obtained nicely. At larger ℓ, the profile from the particle bed approaches the filtered analytical profile more closely, while at the same time the entire profile gets smoothened.

By stretching the particle bed the separation between the spheres is preferentially adjusted along the x-axis of the bed. A measure for this stretching is given by the gradient $\mathrm{d}x_1/\mathrm{d}x_0$, which is plotted in Fig. 5. As a result, the isotropy of the homogeneous particle bed is altered in a very specific manner.

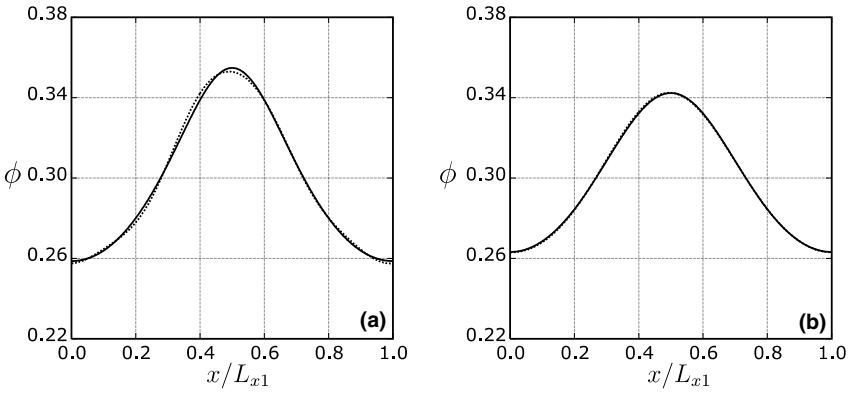

Fig. 4. Comparison between the filtered analytic profile (drawn line) and the filtered profile of the stretched particle bed (dotted line): (a) $\ell = 0.5a$, (b) $\ell = 3a$. In (a) the separate lines can be distinguished, while in (b) the lines practically coincide.

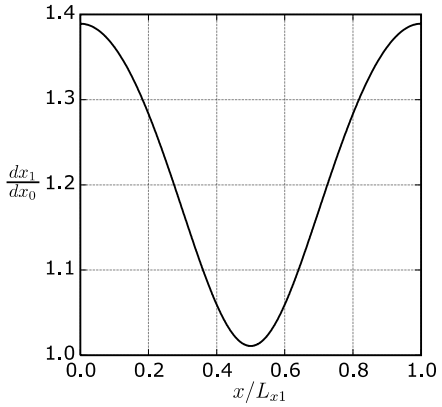

Fig. 5. Stretching ratio $\mathrm{d}x_1/\mathrm{d}x_0$ of the particle bed as a function of position.

In Fig. 6(a) the particle distribution function $g(x,r)$ of the ST bed is given. Here r denotes the radial separation in the y–z plane. The function $g(x,r)$ is normalized with the mean number density and represents an average for the entire bed, based on the ensemble of 50 realizations.

Since spheres cannot overlap, the probability of finding the center of a second sphere at a separation smaller than $2a$ from the center of any sphere is zero. The radius of this exclusion zone is indicated by the circle in the center of the graph. In an ensemble of hard spheres packed at a moderately dense packing, the probability to find a second sphere close to the central sphere is increased. This is indicated by the dark ring close to the exclusion zone. Since this region is preferentially occupied, a second region outside this ring is found where the probability to find a sphere is reduced due to the steric hindrance of the sphere in the first ring around the central sphere. At increasing separation the probability approaches 1.0, indicating that there is no preferential separation distance at large separations. In an isotropic homogeneous system, the alternating pattern of increased and decreased probabilities has to be independent of the primary axes and forms a semi-circle

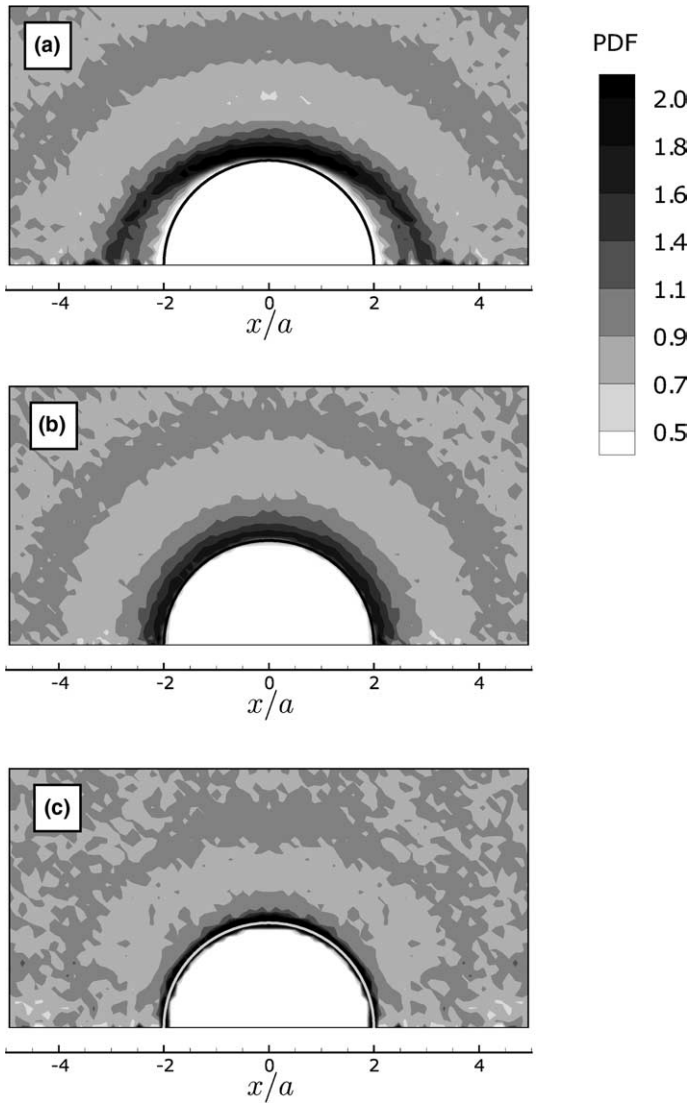

Fig. 6. Particle distribution function $g(x,r)$ of (a) the stretched particle bed, (b) the particle bed generated by inhomogeneous thermalization and (c) the bed generated by fluidization. The x coordinate indicates separation along the x-axis, the r coordinate indicates separation from the x-axis in the y–z plane of the particle bed.

around the center. However, upon stretching of the particle bed, an anisotropy is introduced. The separation between spheres in the stretching direction increases, which reduces the probability to find spheres along the stretching direction. As a result, the shape of the rings of increased and decreased probability has become oval, as is clearly visible in Fig. 6(a).

4.3. The thermalized RND particle bed (TH)

It was shown that the ST particle beds contain a global anisotropy. It was found upon analysis of the simulations, that stretching had a very distinctive impact on the flow and force profiles (see following sections). Therefore we also performed simulations in random particle beds that contained a macroscopic density profile of the same magnitude as that of the stretched bed, but did not contain the typical anisotropic effects that are associated with stretching.

These particle beds (indicated as TH) were generated by thermalization while applying an inhomogeneous body force to the spheres, such that during thermalization the spheres were pushed to the center plane in the x-direction of the box. The ϕ profile obtained via this route is given in Fig. 7. The profile of the body force was determined to obtain a density profile with shape and minimum and maximum values that were comparable to that of the ST bed.

The profile in Fig. 7 shows that the thermalized bed approximates the shape of the stretched density profile reasonably well. (As it will become clear later on, close agreement between these two cases is not required for the purpose of the present study. We simply chose the thermalized RND particle bed to have an ensemble-average voidage profile roughly comparable to that of the ST bed.) The figures show that as the filter length is increased, the profile becomes more smoothened and symmetric and approaches the filtered analytic profile of the ST case. For the TH simulations 100 realizations were used. The main departure from the ST profile is found near the peak and the minimum in the ϕ profiles, where the TH bed is clearly flatter compared to the ST profile.

In Fig. 6(b) the particle correlation function $g(x,r)$ of the TH bed is given. This figure shows clearly that the anisotropic effects of the ST bed are absent in the TH bed. The profiles of alternating low and high probability are circular around the center sphere, which indicates that there is no influence of either the forcing method or of the spanwise box dimensions on the global micro structure of the particle bed, even at larger separations.

4.4. The fluidized RND particle bed (FL)

An inhomogeneous particle bed was also obtained by fluidization of the particles in a numerical simulation. A homogeneous bed of particles inside a periodic domain (having the same dimensions as in the stretched and thermalized bed cases mentioned above) was subjected to a combination of a body force acting both on the particles and the fluid, and a mean pressure gradient which exactly balanced the total body force acting on the

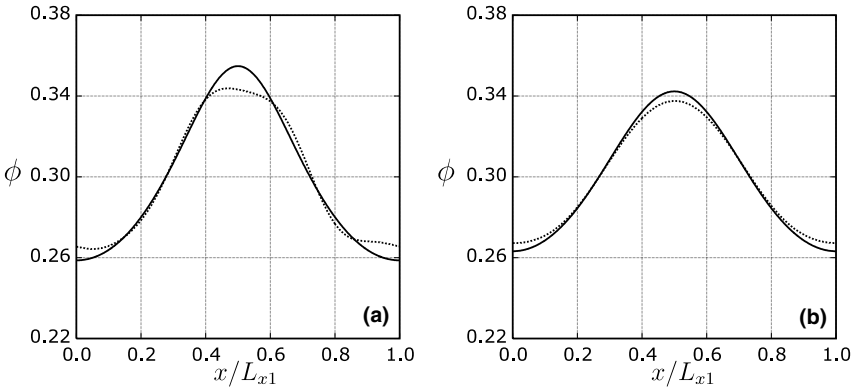

Fig. 7. Comparison between the filtered analytic ϕ profile of the stretched particle bed (drawn line) and the ensemble averaged profile of 100 realizations of the thermally generated particle bed (dotted line): (a) $\ell = 0.5a$, (b) $\ell = 3a$.

fluid–particle mixture. Both the fluid and the particles were allowed to respond to these applied forces. The motion of each particle was followed by integrating Newton's equations for linear and angular momenta. The particle collisions were assumed to be frictionless and elastic. Both normal and tangential lubrication forces were included in the calculations when the particle separation fell below grid resolution. The density of the particles was assumed to be 2.0 times that of the fluid. The details of the simulations are not necessary for the purpose of the present manuscript, and we simply note that an inhomogeneous distribution of particles that took the form of a traveling wave developed spontaneously in these simulations. Such traveling wave solutions are well known in fluidized beds and have been observed experimentally (Duru et al., 2002).

Fig. 8 presents a space–time plot of the particle volume fraction, where the ordinate is the position along the streamwise direction and the abscissa is time. Two copies of the periodic domain are juxtaposed, as is evident from the range of the ordinate in this figure. It can be seen from these figures that at times greater than 1000 (a.u.), the dark band representing the region of high concentration had acquired a nearly steady traveling speed, while the structure continued to evolve in the more dilute region. We obtained fifty realizations of the particle positions in the traveling wave frame shown in Fig. 8. Fixed beds of (stationary) particles located at the positions obtained in these simulations are henceforth referred to as the fluidized RND particle beds (FL). Fluid flow through each realization of the FL beds was performed in the same manner as in the ST and TH beds, by keeping the particles stationary and applying a body force only to the fluid.

The particle volume fraction profile obtained by averaging over the fifty realizations of the FL bed is shown in Fig. 9. The three curves correspond to three different filter lengths used in the averaging process. While the

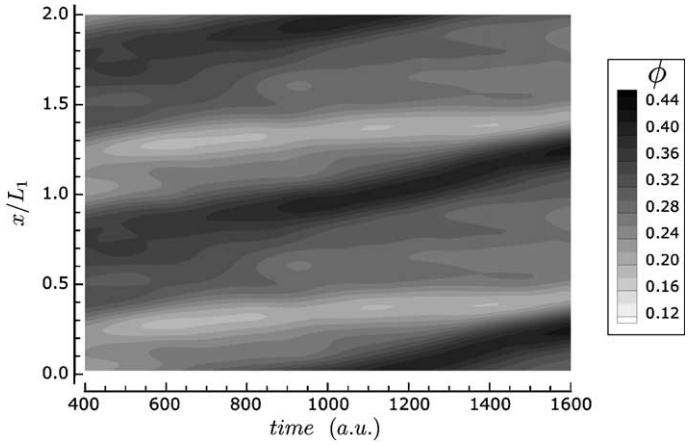

Fig. 8. Time evolution of the volume profile of a traveling density wave. The image shows two times the periodic box length.

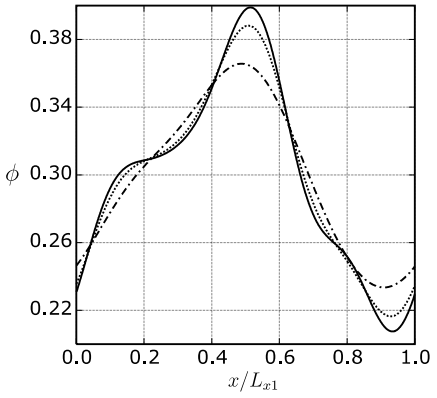

Fig. 9. The filtered volume fraction profile of an ensemble of 50 beds selected from the traveling density wave simulation. The filtering length was varied from $\ell = 0.5a$ (drawn line), to $\ell = 1.5a$ (dotted line), to $\ell = 3.0a$ (dashed-dotted line).

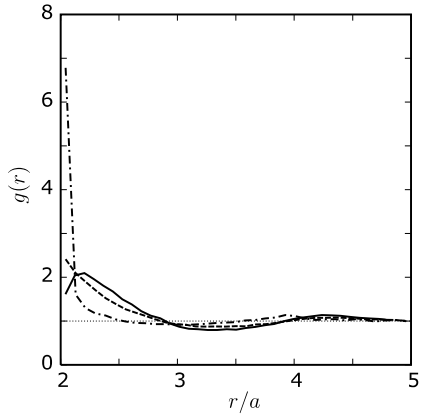

Fig. 10. Radial distribution function $g(r)$ of the ST bed (drawn line), the TH bed (dashed) and the FL bed (dashed dotted).

average volume fraction in the FL beds is the same as those in the ST and TH beds, the volume fraction profile in the FL beds contains more structure (sharper peak, shoulders, etc.). In addition, the microscopic structure of the FL beds is also quite different from the other beds, see Fig. 6(c). The particle distribution function in this case is roughly isotropic (as in the TH beds), but the dark band near contact (i.e. at $r/a = 2$) is noticeably narrower. This typical structure can be traced to the short range hydrodynamic forces (mainly, the lubrication forces).

The data shown in Fig. 6 can be readily collapsed to obtain the radial distribution function, $g(r)$, see Fig. 10. The differences in the microstructure between these three beds are more readily transparent in this figure. The curve representing the TH beds is close to what one would expect for a homogeneous random particle bed at intermediate volume fractions. The value of $g(r)$ near contact is $\approx$2.5 for the TH beds, reaches a minimum at $r/a \approx 2.9$, and a secondary maximum at $r/a \approx 4.3$. Stretching clearly changes the nature of the curve near contact. A sharp increase in the value of $g(r)$ near contact in the FL beds is readily transparent, which also exhibits narrower secondary maximum at $r/a \approx 4.0$.

5. The two-fluid momentum balances

In Section 2 the two-fluid formulation of the momentum balance for flow in the particle bed has been given. In this section it is shown how the momentum balances are affected by the different steps in the averaging procedure and how each of the terms contribute to the momentum balances.

5.1. The effect of filter length ℓ and ensemble averaging

In the two-fluid model the interaction between the solid phase and the fluid is determined by the force $f(x)$ (as it is understood that we will further only examine variations of flow properties in 1D, we will drop the bold vector notation). Eq. (11) shows that $f(x)$ can be obtained directly from the simulations after correction of the force $F(x)$ for the slowly varying pressure profile that develops in the particle bed due to inhomogeneous spatial distribution of the particles. The contour plot of Fig. 11 shows the distribution of pressure in a

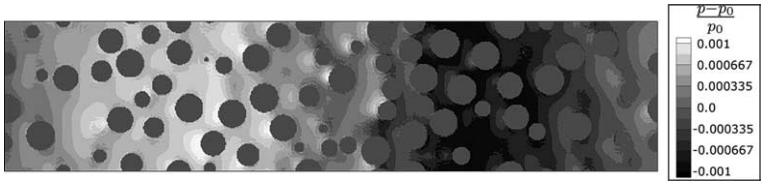

Fig. 11. Contour plot of the pressure distribution in a cross section of a particle bed from the thermalized bed case.

cross-section in one realization of the particle bed simulations. The plot shows that relative to the mean pressure the pressure increases in the left part of the particle bed, since the contour color is generally lighter, while past the maximum particle concentration, on the right side of the bed, the pressure decreases and the contour colors are generally darker. The figure shows that the pressure locally, on the particle scale, can vary considerably.

Fig. 12(a) through (d) show how the slowly varying pressure profile contributes to the profile of the force $F(x)$ as compared to the profile $f(x)$ and it shows the impact of the spatial and ensemble averaging procedures on the resulting force profiles. The forces, as well as all other terms that appear in the momentum balances, to be discussed below, are made dimensionless with the Stokes drag force per unit volume F_{St},

$$F_{\mathrm{St}} = 6\pi\eta a\bar{u}_{x,\mathrm{f}}\bar{n}, \tag{32}$$

where η is the dynamic viscosity and $\bar{n}$ the mean number density in the domain. The force profiles shown in Fig. 12 were obtained for the geometry of the stretched particle bed (ST). Since qualitatively similar behaviour is observed in the other geometries, the ST bed can be considered a representative example for discussing the impact of the averaging procedures.

Fig. 12 shows that the correction on $F(x)$ is substantial. In the center of the bed, at the maximum volume fraction particles, the force $F(x)$ is increased relative to $f(x)$, while near the minimum concentration it is decreased. Since the pressure profile changes from a maximum on the left side to a minimum on the right side of the bed, the pressure gradient obtains the largest negative value at the bed center and largest positive value near the periodic boundary, at the lowest concentration. In the quasi-1D bed, the relation between $F(x)$ and

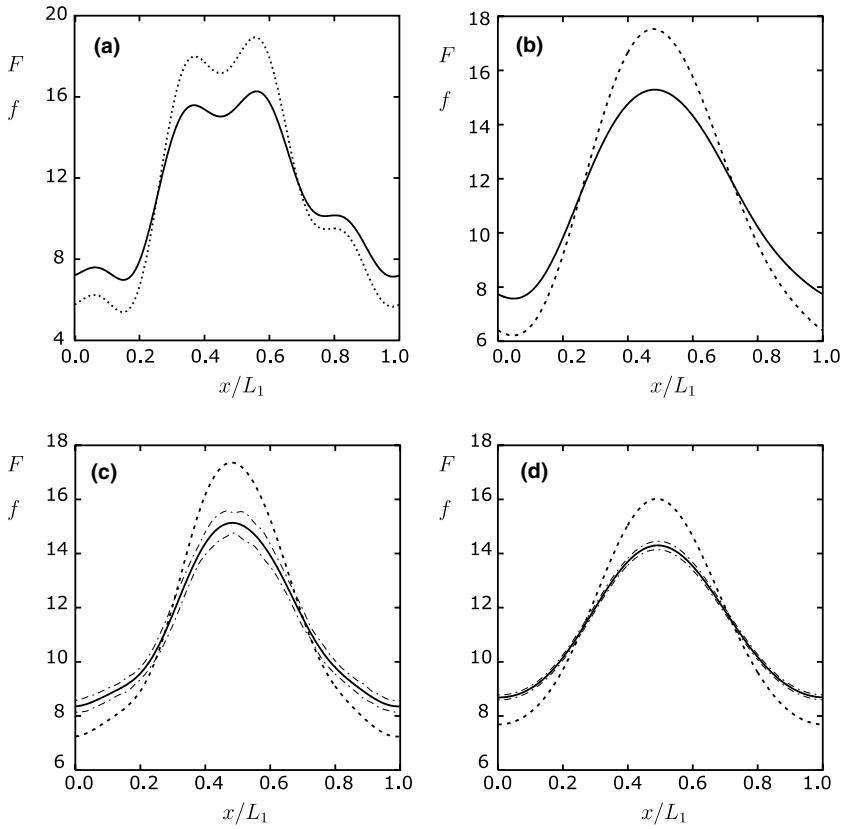

Fig. 12. Profiles of the dimensionless forces $F(x)$ (dashed line) and $f(x)$ (drawn line) in the ST geometry. Variation of filter length; $\ell = 0.5a$ for (a) and (c), $\ell = 3.0a$ for (b) and (d). Figures (a) and (b) show the forces for a single realization of the ST field, figures (c) and (d) give the forces obtained by ensemble averaging over 50 realizations. In figures (c) and (d) the standard error on f is indicated by the thin dashed-dotted lines. (Note, the scale of the y-axis is adjusted for figure (a)).

$f(x)$ becomes $f(x) = F(x) + \phi\, \mathrm{d}p/\mathrm{d}x$, which shows that at negative gradients $f(x)$ should be smaller than $F(x)$, which explains the observed changes in the force profile.

The figure clearly demonstrates the impact of a change in filter length ℓ. With a short filter length, $\ell = 0.5a$, fluctuations in the particle field have a visible impact on the resulting force profiles, clearly present in Fig. 12(a). After ensemble averaging over 50 realizations, these variations have been smoothed out completely. Increasing the filter length also removes these details, even in a single realization. Due to the strong filtering effect at larger ℓ, changing from $\ell = 0.5a$ to $\ell = 3.0a$ also reduces the variance of the ensemble averaged force profile, shown by the decreased standard error.

The averaging of the particle beds draws the force profiles towards their mean value and extremes are suppressed. With short filter lengths ℓ, details are preserved, but also the range of the forces becomes wider. This is shown by the larger scale of the y-axis in Fig. 12(a). Ensemble averaging suppresses these fluctuations, but with a short filter length, more realizations are required to obtain a smooth profile.

5.2. The fluid phase momentum balance

The value of each term of the fluid phase momentum balance of Eq. (4) can be determined from the simulations as a function of location. In the steady flow studied here, the fluid phase momentum balance consists of six terms that in 1D can be written as

$$\underbrace{(1-\phi)\rho_{\mathrm{f}} u_{\mathrm{f}} \frac{\mathrm{d}u_{\mathrm{f}}}{\mathrm{d}x}}_{\mathrm{I}} = \underbrace{-(1-\phi)\frac{\mathrm{d}p}{\mathrm{d}x}}_{\mathrm{II}} \underbrace{-\frac{\mathrm{d}(\rho_{\mathrm{f}}(1-\phi)\overline{u_{\mathrm{f}}' u_{\mathrm{f}}'})}{\mathrm{d}x}}_{\mathrm{III}} \underbrace{T_1 + T_2}_{\mathrm{IV}} \underbrace{-f}_{\mathrm{V}} + \underbrace{(1-\phi)\rho_{\mathrm{f}} g}_{\mathrm{VI}}. \tag{33}$$

The terms in this balance are the fluid inertia term (I), the pressure gradient term (II), the Reynolds stress term (III), the fluid–particle stress term (IV), the interphase interaction force term (V) and the body force term (VI). Here T_1 and T_2 are used to indicate the first and second order terms of the fluid particle stress.

Fig. 13(a) shows that terms II, V and VI are the dominant terms of the momentum balance. This figure shows that the body force term that imposes the fluid motion is a constant positive term that varies slowly with volume fraction. This term is predominantly balanced by the interphase interaction force and the slowly varying pressure gradient. The pressure gradient term varies slowly around zero and has also a zero mean value. As the figure shows, the residual of these three terms is more than one order of magnitude smaller. This residual is the result of the remaining terms, the fluid inertia, Reynolds stresses and particle stress T. In Fig. 13(b) these small terms are plotted. It is interesting to notice the correspondence between the Reynolds stress term, III and the inertial term I. Generally, the sign of III is roughly the opposite of the inertial term

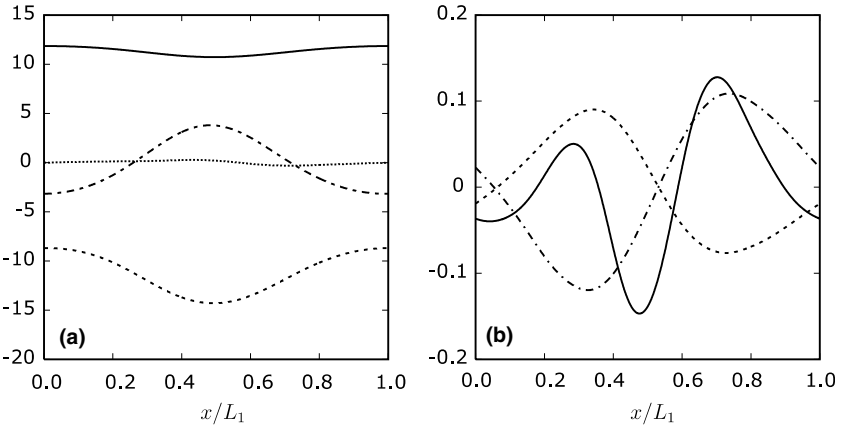

Fig. 13. Profiles of the various dimensionless terms of the fluid momentum balance in the ensemble average of the ST geometry. (a) Major terms, the body force term (VI, drawn line), the interphase interaction force term (V, dashed line), the pressure gradient term (II, dashed-dotted line) and the sum of the three terms (dotted line). (b) The minor terms, i.e. the inertia term (I, dashed line), the Reynolds stress term (III, dashed-dotted line) and the T term (IV, drawn line). (Filter length $\ell = 3.0a$).

while the shape is roughly the same. This was also noticed in the other geometries. As the inertial terms contribute very little to the force balance (33), one can readily expect that the added mass force term will also be quite small. For example, a reasonable first estimate of the added mass force is $\frac{1}{2}\phi\rho_f u_f \, du_f/dx$, which is comparable to term I. With this in mind, in the ensuing discussion, we will simply refer to f as the drag force.

Fig. 14 shows the role of the T terms in closing the momentum balance. In this figure the interphase interaction force profile $f(x)$, obtained directly from the particle phase, is indicated with the dashed line. This profile is compared to the force profile $f(x)$ from the fluid phase momentum balance, where each term was computed directly from the flow field and the balance was rewritten explicitly in $f(x)$. When all terms in the momentum balance are present, both routes should yield identical force profiles and the lines should overlap perfectly. In Fig. 14(a), the particle–fluid stress terms T were omitted. This figure shows that there is a small discrepancy between the two force profiles, indicating that some terms in the balance are missing. Adding terms T_1 and T_2 gradually improves the correspondence between the two profiles. In Fig. 14(b) the force profile with T_1 is plotted while in Fig. 14(c) the two terms T_1 and T_2 are included. We chose to portray these effects using a single realization of the ST bed, since for any single realization the spatially averaged momentum balance should already be closed. For profiles obtained with larger values of ℓ (e.g. Fig. 13) the contribution of the T terms has become even smaller than in this example. The magnitude of the particle–fluid phase stress terms changes with $\mathcal{O}(a/\ell)$ which shows that the magnitude of these terms is largest for small ℓ values. At $\ell = 0.5a$ improvement of the force profiles is demonstrated when up to second order terms are included. From a practical point of view, the contributions of T_1 and T_2 can clearly be ignored.

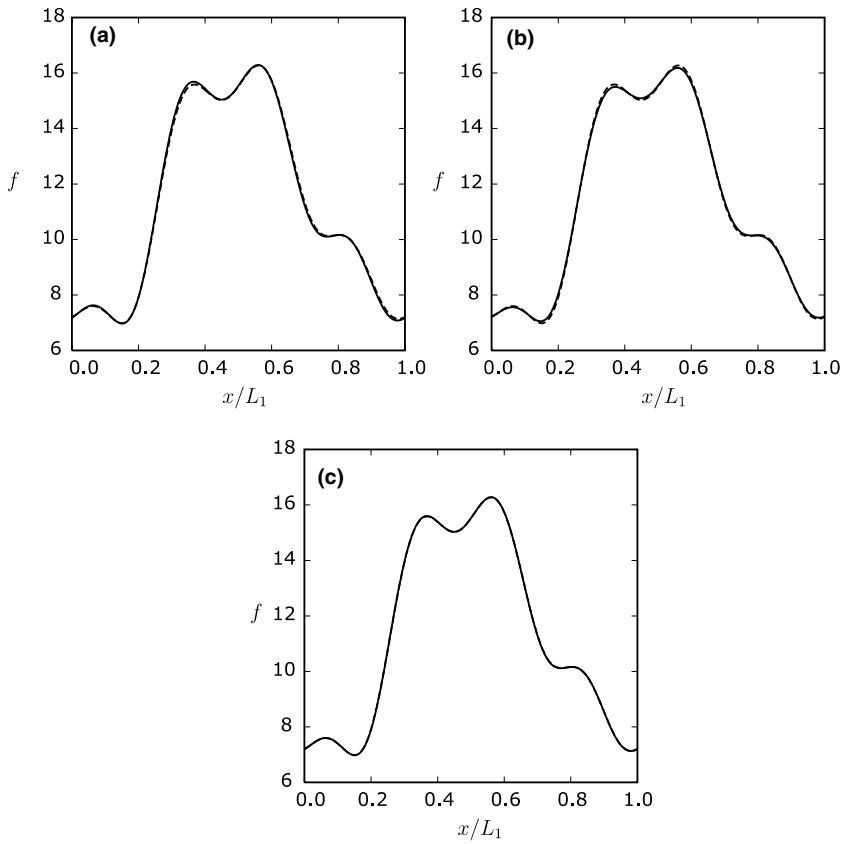

Fig. 14. Comparison of the dimensionless drag force profiles f obtained from the particles and from the fluid momentum balance with (a), no T-terms, (b) only T_1 and (c) with $T_1 + T_2$. The drag force obtained from the particle phase (dashed line) overlaps almost exactly with that estimated from the fluid phase (drawn line). Slight departure between these two lines is noticeable in figures (a) and (b), but not in figure (c). Single ST bed, $\ell = 0.5a$.

6. Modeling the drag force

In this section the force profiles obtained from the different geometries are studied to asses the relation between the local drag force $f(x)$ and local bed properties such as the volume fraction of particles. All simulations were done at a constant particle Reynolds number of $Re_p = 2a\bar{u}_{x,f}/\nu = 20$.

6.1. Drag force in the ST particle bed

In Fig. 15(a)–(c), the continuous drawn line shows the force profile $f(x)$ in the ST bed, as determined with three different values of the filter length ℓ (the profiles in Fig. 15(a) and (c) are identical to $f(x)$ in Fig. 12(c) and (d)). The force profiles $f(x)$ in Fig. 15 are compared to two different closure models that were determined empirically from simulations of homogeneous particle beds.

The first type of closure is given in Fig. 16. The circle points and drawn line indicate the $f - \phi$ relation obtained from homogeneous randomized beds of particles at constant Reynolds number (errorbars have been omitted since the standard error is smaller than the symbols). The second order polynomial

$$f(\phi) = A\phi^2 + B\phi + C \tag{34}$$

has been fitted through these data points to capture the relation between volume fraction and force.

The dotted curve in Fig. 15(a)–(c) shows the resulting force profile as predicted by the empirical $f(x)$ relation after inserting the volume fraction profile $\phi(x)$ of the particle bed into the empirical polynomial relation of the

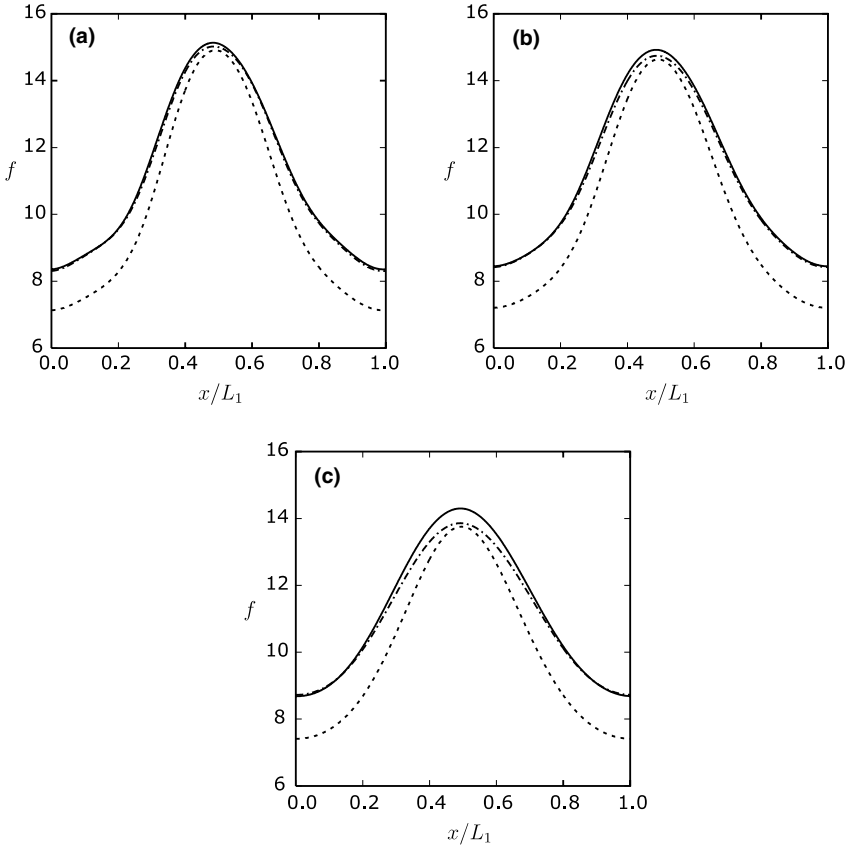

Fig. 15. Dimensionless drag force f profile in the ST bed. Simulation (drawn line) compared with locally homogeneous model (f at $dx_1/dx_0 = 1.0$, dotted line) and $f = f(\phi, dx_1/dx_0)$ (dashed-dotted line) model. Variation of (a) $\ell = 0.5$, to (b) $\ell = 1.5$ to (c) $\ell = 3.0$. In figure (a), the drawn and the dashed-drawn lines overlap almost exactly, while in figures (b) and (c), some departure between these two curves can be seen near the peak.

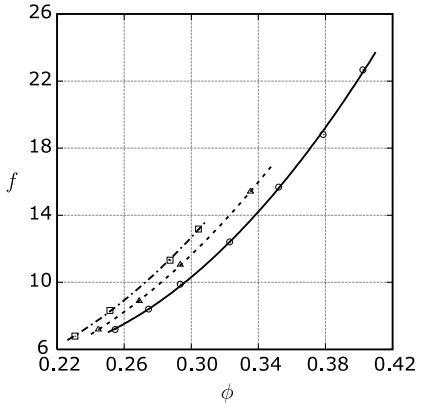

Fig. 16. Datapoints and interpolated curve of the dimensionless drag force f obtained from homogeneous simulations with no stretching, i.e. $dx_1/dx_0 = 1.0$ (⊙, drawn line), and with stretching at $dx_1/dx_0 = 1.2$ (△, dashed line) and $dx_1/dx_0 = 1.4$ (□, dashed-dotted line).

drag force (i.e. plotting $f(\phi(x))$). The main observations are that towards the center of the particle bed the force is predicted adequately, while towards the boundaries the force is systematically under predicted.

We now show that the clear deviations between between the empirical prediction and the actual simulation of the force profile originates in the manner in which the density profile in the particle bed has been generated. The inhomogeneous particle beds were created by extending the spacing between the particles in the streamwise direction. This bed extension is characterized by the gradient dx_1/dx_0 which, as shown in Fig. 5, varies locally between 1.0 and 1.4. The deviations between simulated and predicted drag force are the largest at the location where dx_1/dx_0 is largest.

To asses the impact of streamwise extension on the drag force, homogeneous bed simulations were done where the entire bed was expanded homogeneously. The dashed line and corresponding data points in Fig. 16 show the $f-\phi$ relation at $dx_1/dx_0 = 1.2$ while the dashed-dotted line was obtained at $dx_1/dx_0 = 1.4$. The figure shows indeed that extension has the effect to increase the volume averaged drag force. These two curves were also interpolated with a quadratic polynomial function.

To capture the impact of both the volume fraction and the bed extension in a single relation, the three curves in Fig. 16 were interpolated with a single polynomial function as,

$$f(\phi, dx_1/dx_0) = p_1(dx_1/dx_0)\phi^2 + p_2(dx_1/dx_0)\phi + p_3(dx_1/dx_0), \tag{35}$$

where the parameters p_i vary with dx_1/dx_0 as

$$p_i(dx_1/dx_0) = a_i(dx_1/dx_0)^2 + b_i(dx_1/dx_0) + c_i. \tag{36}$$

In Fig. 15 the force profile based on this closure model has been plotted by the dashed-dotted line. In all three curves the deviation at the extremes of the particle bed has now been removed and the force profile is accurately predicted. This demonstrates that the dominant effect in the deviation between the two curves is a result of the inhomogeneous bed extension.

Although the profiles are generally well captured, some differences as a function of ℓ remain. At larger filter lengths a systematic deviation arises between the predicted and the simulated force profile at the location of maximum ϕ. With increasing ℓ, the relatively narrow peak in ϕ gets smoothed rapidly. Since the $f-\phi$ relation is quadratic, the sensitivity for variations in ϕ is greatest at larger values of ℓ, as observed at the maximum in ϕ, i.e. in the center of the particle bed.

6.2. Drag force in the TH bed

Since there was a strong impact of the small scale structure of the ST bed on the resulting force profile, we simulated the flow in the inhomogeneously thermalized TH particle bed. It was anticipated that although this bed possesses a large scale structure, the microscopic structure would become practically isotropic. It then was

expected that the force profile would not be dependent on stretching effects and the resulting force can be predicted with a force closure that is based on a locally homogeneous force model.

In Fig. 17(a)–(c), $f(x)$ is plotted for the TH bed (drawn line), together with the prediction of the force profile based on the locally homogeneous approximation (dashed line). The locally homogeneous model is the closure as obtained from the quadratic interpolation of the $f-\phi$ relation for $\mathrm{d}x_1/\mathrm{d}x_0 = 1.0$ (see drawn line in Fig. 16). The prediction of the force profile based on the locally homogeneous model is reasonably adequate. The large deviation observed in the ST bed due to stretching effects is now lifted and the force profile captures the general trends. The main deviation is that the prediction has a tendency to overestimate the force profile both in the maximum and the minimum of the density profile. This overestimation is larger than the interval of the standard error on $f(x)$ (thin dashed-dotted line). Although the overestimation appears to decrease at larger values of ℓ, it remains clearly present.

The deviation between the simulated and the predicted force profile indicates that there are (small) terms missing in the closure model. In the literature (e.g. Foscolo and Gibilaro, 1984), suggestions have been made that additional closure terms are required that contain the gradient of the volume fraction, $\nabla\phi$. However, if this was the case in the current simulations, then the main deviations would be observed in the profile at the location where the gradients are strongest, while also a fore-after asymmetry around the center plane of the particle bed would be observed in the flow direction, due to a sign-change in the gradient of ϕ. These effects are not observed in the force profiles, since the best prediction is found at the part where the gradients are largest, and no indication for a substantial fore-after asymmetry is present, other than slight wiggles in the profile of Fig. 17(a), due to the short filter length. Alternatively it might be suggested that second order gradient terms,

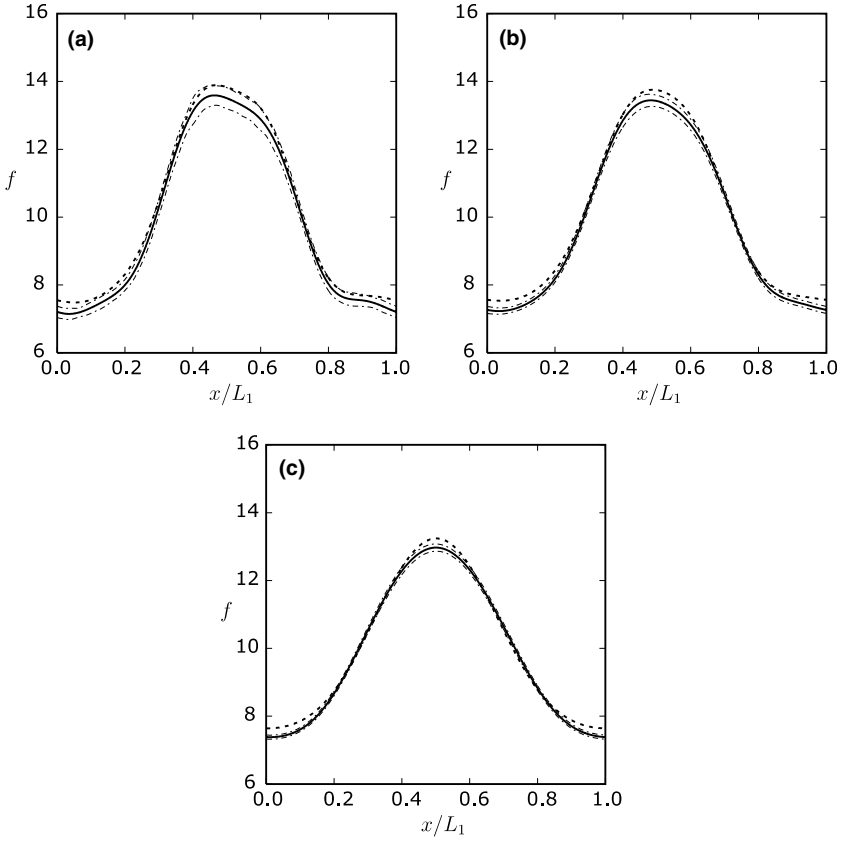

Fig. 17. Dimensionless drag force profile in the TH bed. Simulation (drawn line) with standard error (thin dashed-dotted lines) compared with locally homogeneous model (f at $\mathrm{d}x_1/\mathrm{d}x_0 = 1.0$, dashed line). Variation of (a) $\ell = 0.5$, to (b) $\ell = 1.5$ to (c) $\ell = 3.0$. From figure (a) to (c) the locally homogeneous model gives the best approximation at the steepest part of the force curve, while the prediction at minimum and maximum value approaches the drawn line with increasing ℓ.

$\nabla^2\phi$, are missing from the closure. However, this is not the case either. The second derivative of the ϕ-profile is positive on the outside and negative in the center. This would lead to opposite corrections between the center and the outsides of the particle bed, while the actual profile is overestimated in both these regions. Higher order concentration gradients become so small in magnitude that it is not expected that they would lead to any further significant contribution in the absence of first and second order effects. Therefore, these simulation results do not support any closure that may contain ϕ-gradient effects.

The origin of the overestimation is probably also a result of the manner in which the particle bed was generated. The ST simulations have already demonstrated a high sensitivity of the force profile to effects of the microscopic structure of the particle bed. Since a inhomogeneous body force was applied to the particles during thermalization to create the density profile, it is not guaranteed that via this route the microscopic structure of the bed is locally identical to that of a truly homogeneous bed. As can be seen in the ϕ profile at $\ell = 0.5a$ (Fig. 7), in the center and on the outside the ϕ-profile is relatively flat over a substantial length of the bed. If, due to the inhomogeneous body-force, collisions in the flow-direction are enhanced, then a (small) increase in the separation in the streamwise direction may be present. As the homogeneous stretched beds already showed, a small increase in separation in the streamwise direction may already have a significant impact on the resulting force profile. Unfortunately, the radial distribution function (Figs. 6 and 10) does not provide strong evidence for this hypothesis. The radial distribution functions are based on all particles present in the bed and subtle local effects are averaged out.

6.3. Drag force in the FL particle bed

In Fig. 18, the $f(x)$ profile of the FL particle bed is given. Again, from Fig. 18(a)–(c) the filter length is increased. The general shape of the force profile corresponds to the $\phi(x)$ profile shown in Fig. 9. The dashed line in Fig. 18 shows the prediction of the force profile based on the empirical drag relation of the homogeneous beds at $dx_1/dx_0 = 1.0$ (see drawn line in Fig. 16). The locally homogeneous model generally under-predicts drag force, the departure being larger than the standard deviation of the force profile obtained through the simulations.

As was shown by the radial distribution function in Fig. 10, there is a clear difference in microstructure between the FL particle bed and the TH particle bed. In the simulation that was used to generate the FL bed, short range hydrodynamic interaction forces are present that result in a redistribution of particles, such that particles tend to collect at short separations. The role of the short range hydrodynamic forces can be verified readily as follows.

Recall that the various realizations of particle configurations in random homogeneous beds were constructed by giving the particles in a periodic box an initial random velocity and allowing the particles to move around as elastic hard spheres in the absence of any interstitial fluid. Sample configurations were gathered at various times during the ensuing transients. In the actual fluid flow simulations used to find the drag force, the particles were held stationary. The drawn line in Fig. 16 was obtained in this manner. In order to obtain a modified microstructure for the homogeneous beds, we took each of these particle configurations and the corresponding particle velocities, and allowed the system to quench itself through the introduction of the lubrication force. This retained the homogeneity of the beds, but changed the radial distribution function; specifically, the magnitude of $g(r)$ at close separations increased sharply. Beds generated in this manner will be referred to as modified homogeneous beds. Fig. 19(b) shows the radial distribution of a modified homogeneous bed at $\phi = 0.3$ (dashed-dotted line). Also shown in this figure as the drawn line is the radial distribution function of the FL bed. Both curves rise steeply at close separations (r/a approaching 2), and manifest the same small peak near $r/a = 4$. Thus, the origin of the large value of $g(r)$ near contact in the case of the FL bed is now clear.

The drawn line in Fig. 19(a) represents the dimensionless drag force at different particle volume fractions (and a Reynolds number of 20) obtained in a random homogeneous bed, and this line was presented previously in Fig. 16. Dimensionless drag forces computed under identical flow conditions in the modified homogeneous beds are shown in Fig. 19(a). There is a very clear effect of the microstructure on the computed drag force. Stretching a random homogeneous bed led to a decrease in the magnitude of $g(r)$ at close separations and an increase in the drag force (see Figs. 10 and 16). Increasing the magnitude of $g(r)$ at close separations

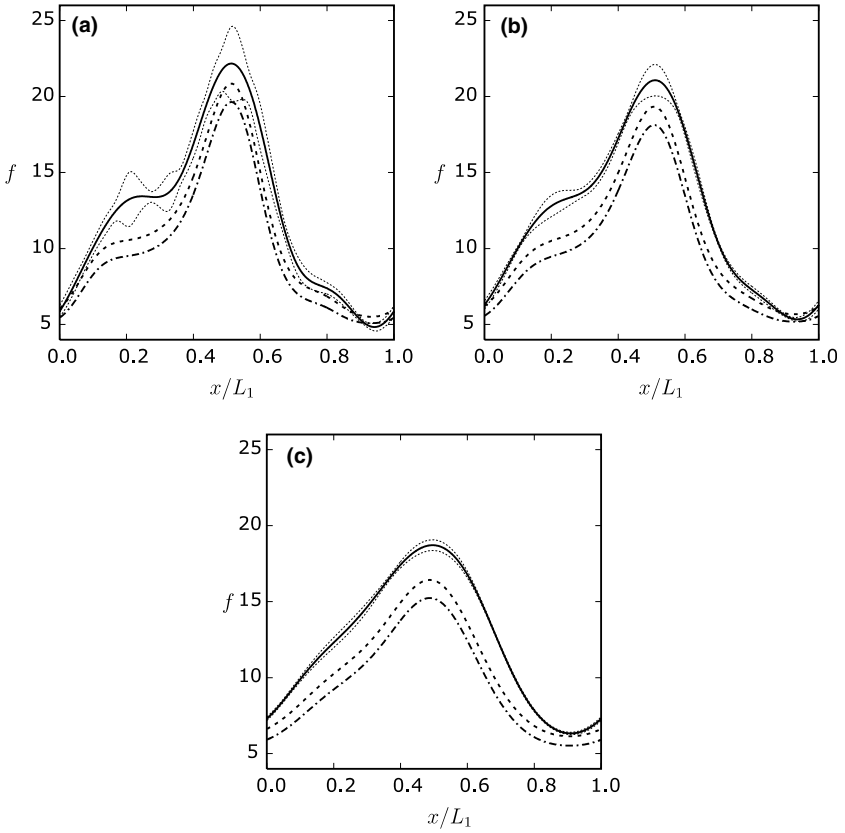

Fig. 18. Dimensionless drag force profile in the FL bed. Simulation result (drawn line) with standard error (thin dotted lines) compared with locally homogeneous model (dashed line) and locally homogeneous model with modified microstructure (dashed-dotted line): (a) $\ell = 0.5$, (b) $\ell = 1.5$ and (c) $\ell = 3.0$.

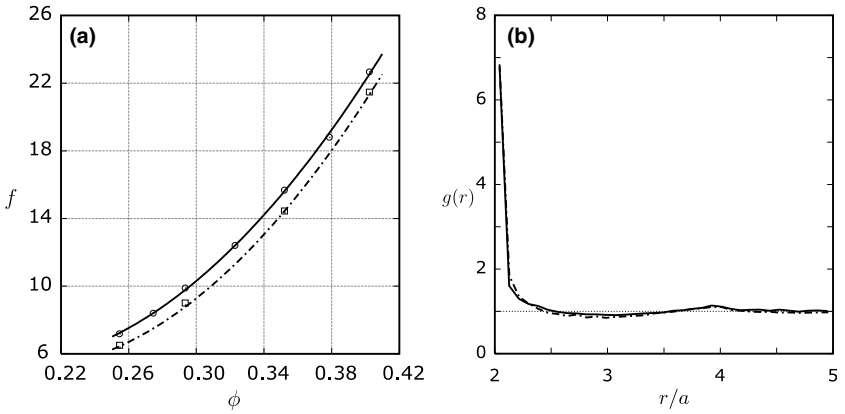

Fig. 19. (a) Datapoints and interpolated curve of f for homogeneous particle bed with unmodified (drawn line) and modified (dashed line) microstructure. (b) Radial distribution function $g(r)$ of fluidized wave simulation (drawn line) and homogeneous thermalized bed with modified microstructure (dashed-dotted line) at $\phi = 0.3$. The two lines nearly overlap for all values of r/a and approach a similar value near contact.

has the exact opposite effect. The effect shown in Fig. 19(a), however, does not explain the difference between the simulation results (drawn line) and the locally homogeneous model (dashed line) seen in Fig. 18. If we

replace the locally homogeneous model (i.e. the drawn line in Fig. 19(a)) with the locally modified homogeneous model (dashed line in Fig. 19(a)), we obtain the dashed-dotted line shown in Fig. 18, which clearly exacerbates the discrepancy. Thus, additional effects must be brought in to explain the discrepancy.

Quite obviously, the local microstructure is anisotropic in the macroscopically one-dimensional flow obtained in the fluidized bed. Some evidence for this anisotropy can be seen in Fig. 6(c), while both the homogeneous and modified homogeneous beds would have no anisotropy. Fig. 6(c) suggests that in the FL beds, the particles tend to collect more in the lateral direction (planar arrangement of particles) with a slight decrease in the value of $g(x,r)$ in the streamwise direction (behind or in front of the test particle). Such a configuration, should it occur, will indeed increase the drag force. However, this remains only a speculation at the present stage.

7. Summary

In most fluid–particles of practical interest, such as those obtained in fluidized suspensions, inhomogeneous distributions of particles arise frequently. Traveling waves and bubble-like voids in fluidized beds are common examples of such inhomogeneities, and simulation of such spatiotemporal structures through two-fluid models has been the subject of many studies. Closure relations needed for the two-fluid models are deduced from experiments or derived from detailed analysis of nearly homogeneous suspensions. Among the terms requiring closure, the drag force between the fluid and particle phases is the most important one. Commonly used closure relations express the drag force in terms of local particle volume fraction and the local slip velocity between the two phases. In the present study, we set out to examine how good this assumption is for inhomogeneous beds. We created particle assemblies in a periodic box in several ways.

Various realizations of *homogeneous* assemblies were created by allowing the particles to move around randomly while experiencing elastic collisions and no effect of the interstitial fluid. *Modified homogeneous* beds were also created by allowing the randomly moving particles to be brought to rest through short range hydrodynamic force due to the interstitial fluid. The radial distribution functions for these homogeneous and modified homogeneous beds are appreciably different, with the latter showing appreciable enhancement of particles at close separations, which in turn led to a very definite decrease in the drag force (Fig. 19(a)).

We also stretched the homogeneous beds uniformly in one direction (which was also the flow direction in the fluid flow simulations) to create *stretched homogeneous beds*. Such stretching clearly altered the microstructure; in particular, the magnitude of the radial distribution at close separations decreased and anisotropy developed in the radial distribution function. We have shown that the stretching led to an increase in the drag force (Fig. 16). Although we have not presented the results in this manuscript, we have also taken structured beds (simple cubic and face-centered-cubic arrangements) and subjected them to stretching in one direction. We found that stretched beds created in this manner led to higher drag force (for a fixed superficial velocity of the fluid through the bed) when compared to a structured bed of comparable mean volume fraction of particles.

We created inhomogeneous beds in many ways. By stretching the homogeneous random beds non-uniformly, we created stretched *inhomogeneous* beds. From detailed simulations of fluid flow through many realizations of such beds, we first examined the magnitude of each of the terms in the two-fluid model equations. To this end, we employed the filtering operations exactly as they are done in formulating the averaged (two-fluid) equations of motion. In the presence of inhomogeneous distribution of particles, the filter length will obviously have an effect on the estimated profiles of various quantities when the filter length becomes comparable to the length scale over which gradients are present. Hence a careful documentation of the filtering step and the effect of the filter size on the results are included to separate the effect of filter length from those associated with the inhomogeneities. We extracted the axial variation of the fluid–particle drag force in such stretched inhomogeneous beds from fluid flow simulations at a fixed superficial velocity of the fluid. We found that this drag force result could be explained by a model constructed from simulations in stretched homogeneous beds, but not by a model constructed from fluid flow simulations in truly homogeneous beds. We saw no evidence in this calculation for the need for terms involving gradients in particle volume fraction (or equivalently gradients in the slip velocity).

We also created thermalized inhomogeneous beds by allowing the particles to move around (as we did in constructing realizations of the homogeneous beds), except that we now had an axial-position-dependent body force whose effect was to distribute the particles inhomogeneously. We found that in this case, the spatial variation of the drag force could be reasonably well described by a model constructed from fluid flow simulations in truly homogeneous beds; although some discrepancy was found, it was not consistent with terms involving gradients in particle volume fraction (or equivalently the slip velocity). Instead, it is more likely that this small discrepancy was due to small differences in the radial distribution function in the inhomogeneous and the homogeneous beds.

One-dimensional traveling waves are the simplest of the inhomogeneities in fluidized beds and such a traveling wave can be generated through simulation of fluidization in a periodic box. In the traveling wave frame, the particle volume fraction profile is statistically steady, and we obtained realizations of particle configurations by sampling the wave at various times. Strictly speaking, the wave is never fully developed in microscopic simulations and the standard deviation of the particle volume fraction profile obtained here is larger than those obtained in the stretched and thermalized inhomogeneous beds. The microstructure of particle assemblies obtained in this manner revealed a significant enhancement of the radial distribution function at close separations, just as in the modified homogeneous beds; hence, this enhancement was attributed to short range hydrodynamic forces. (Inelastic collisions between the particles should also have a similar effect, although we did not investigate it in our study.) The spatial variation of drag force in inhomogeneous fixed beds whose particle configurations are the same as those in the traveling wave departed significantly from the predictions of models constructed from simulations through homogeneous and modified homogeneous beds. Yet, there is no evidence for the need for a correction involving gradients in particle volume fraction (or slip velocity). We speculate that this discrepancy is largely due to anisotropy in the particle microstructure, but this issue remains unresolved.

In any case, our study has shown clearly that a departure from a truly random microstructure can have an appreciable effect on the closure for the drag force. Typically, one assumes in two-fluid model calculations that the local drag force can be expressed in terms of the local particle volume fraction and local slip velocity, and this inherently assumes that the particle volume fraction sets the microstructure; this is true for a random configuration. However, anisotropy is common in most flow problems where short range hydrodynamic forces (and inelastic collisions) are also present; and small or large departures in microstructures can come about. When this happens, the drag force closure can become inaccurate. Indeed, the changes in the magnitude of the drag force associated with the changes in microstructure are comparable to or even larger than the typical magnitudes of many of the terms in the fluid phase balance equations: the inertial term, the pseudo-turbulent stress term (resembling a Reynolds stress term) and the fluid–particle stress term (I, III and IV in Eq. (33), respectively); the same can be said about the added mass term and the Faxén terms, which we did not elaborate in this manuscript.

Marchioro et al. (2000, 2001) and Wang and Prosperetti (2001) consider several types of low Reynolds number flows involving particle assemblies with small spatial inhomogeneities (in an ensemble average sense): sedimentation, flow through porous media, shear flow and particle rotation resulting from externally imposed couples. They point out how new terms arise in the closure relations because of the presence of spatial gradients, including a non-Newtonian flow character for the mixture. The analysis by Wang and Prosperetti (2001) of flow through porous media is the one most directly relevant for the present study. It is difficult to make any quantitative comparison between our results (corresponding to $Re = 20$) and those obtained by Wang and Prosperetti (2001) for low Reynolds number flows. Hence, we compare and contrast these two studies only qualitatively.

The series of papers by Prosperetti & coworkers clearly shows that, in the presence of spatial gradients, corrections are needed for the effective stresses. In our simulations, we found that the contribution of the deviatoric stress is very small compared to the drag force, and so we are unable to directly assess the impact of gradients on the deviatoric stress. The presence of a gradient in particle volume fraction certainly influences the pressure field in both studies, and this is readily understandable. The drag coefficient varies with position as a result of the volume fraction gradient in both studies. Wang and Prosperetti (2001) provide an analytic expression for this variation, which is valid in the limit of low Reynolds numbers and small inhomogeneities; see their equation (5.21). In our case, neither is small and so we cannot use these expressions directly.

The studies by Mo and Sangani (1994) and Prosperetti and coworkers clearly show that the spatial variation of the drag force in inhomogeneous suspensions (in the Stokes flow regime) is related to the structure factor and an effective viscosity, which depend on volume fraction. Our studies on stretched beds clearly show the influence of the particle configuration (and hence the structure factor) on the drag force. In both thermalized and stretched beds, the spatial variation of the drag force extracted from our simulations is reasonably well approximated by a locally homogeneous model based on drag coefficients for appropriately chosen homogeneous beds. This is somewhat surprising as the expression deduced by Wang and Prosperetti (2001) differs from a locally homogeneous model.

In sedimenting or fluidized assemblies where the particles are allowed to both translate and rotate the drag coefficients can be very different from those in fixed beds (Saffman, 1973; Wang and Prosperetti, 2001; Wylie et al., 2003). Hence, it would be useful to verify the effect of spatial gradients in particle volume fraction on the interphase interaction force separately for the case of mobile particles.

Finally, we note that the practice of evaluating the drag force closures from direct simulations of flow through random assemblies of particles (e.g., see Hill et al., 2001a) is perhaps most suitable for gas–particle flows where the particle-to-gas density ratio is large and the particle Stokes numbers are very large. In liquid–solid suspensions, where the lubrication forces can have a significant effect on the microstructure, drag force models generated via direct simulations of flow through random assemblies of particles may be inadequate. Even in gas–particle suspensions, where spatiotemporal structures are abundant and, rapid compaction and dilation of assemblies occur frequently in an anisotropic manner, the microstructure may not have enough time to equilibrate into a nearly isotropic configuration; if this is the case, then the drag force closures could become inaccurate.

Accounting for the effect of changes in the microstructure on the drag force in two-fluid models is clearly very complex. It could perhaps involve an evolution equation for the radial distribution function and a drag force closure that incorporates the effect of the local microstructure. This is a formidable problem and may never get tackled. However, it is hoped that the present study has made it clear that when two-fluid model predictions do not agree with experimental (or other simulation) data, one should examine the accuracy of the drag closure.

Acknowledgements

This work was supported by grants from The New Jersey Commission on Science & Technology and The Exxon Mobil Research & Engineering Company. We gratefully acknowledge many helpful discussions with Professor Jos Derksen, who also generated for us realizations of particle configurations from a simulation of a traveling wave in a fluidized bed.

References

Anderson, T., Jackson, R., 1968. Fluid mechanical description of fluidized beds. stability of the state of uniform fluidization. Ind. Eng. Chem. Fundam. 7, 12–21.

Batchelor, G.K., 1988. A new theory of the instability of a uniform fluidized bed. J. Fluid Mech. 193, 75–110.

Chen, M., Kontomaris, K., McLaughlin, J.B., 1998. Direct numerical simulation of droplet collisions in a turbulent channel flow. Part I: Collision algorithm. Int. J. Multiphase Flow 24 (7), 1079–1103.

Chen, S., Doolen, G.D., 1998. Lattice Boltzmann method for fluid flows. Ann. Rev. Fluid Mech. 30, 329–364.

Chopard, B., Droz, M., 1998. Cellular Automata Modeling of Physical Systems, first ed. Cambridge University Press, Cambridge, England.

Dazhi, Y., Mei, R., Luo, L.-S., Shyy, W., 2003. Viscous flow computations with the method of lattice Boltzmann equation. Prog. Aerospace Sci. 39, 329–367.

Duru, P., Nicolas, M., Hinch, J., Guazelli, E., 2002. Constitutive laws in liquid–fluidized beds. J. Fluid Mech. 452, 371–404.

Eggels, J.G.M., Somers, J.A., 1995. Numerical simulation of free convective flow using the lattice-Boltzmann scheme. Int. J. Heat Fluid Flow 16, 357–364.

Foscolo, P., Gibilaro, L., 1984. A fully predictive criterion for the transition between particulate and aggregate fluidisation. Chem. Eng. Sci. 39, 1667.

Glasser, G.J., Kevrekidis, I.G., Sundaresan, S., 1996. One- and twodimensional travelling wave solutions in gas-fluidized beds. J. Fluid Mech. 306, 183–206.

Glasser, G.J., Kevrekidis, I.G., Sundaresan, S., 1997. Fully developed travelling wave solutions and bubble formation in fluidized beds. J. Fluid Mech. 334, 157–188.

Hill, R.J., Koch, D.L., Ladd, A.J.C., 2001a. The first effects of fluid inertia on flows in ordered and random arrays of spheres. J. Fluid Mech. 448, 213–241.

Hill, R.J., Koch, D.L., Ladd, A.J.C., 2001b. Moderate-Reynolds-number flows in ordered and random arrays of spheres. J. Fluid Mech. 448, 243–278.

Jackson, R., 1997. Locally averaged equations of motion for a mixture of identical spherical particles and a newtonian fluid. Chem. Eng. Sci. 52 (15), 2457–2469.

Jackson, R., 2000. The Dynamics of Fluidized Particles, first ed. Cambridge University Press.

Kandhai, D., Derksen, J.J., Van den Akker, H.E.A., 2003. Interphase drag coefficients in gas–solid flows. AIChE J. 49 (4), 1060–1065.

Ladd, A.J.C., 1994a. Numerical simulations of particulate suspensions via a discretized Boltzmann equation. Part 1: Theoretical foundation. J. Fluid Mech. 271, 285–309.

Ladd, A.J.C., 1994b. Numerical simulations of particulate suspensions via a discretized Boltzmann equation. Part 2: Numerical results. J. Fluid Mech. 271, 311–339.

Ladd, A.J.C., 1997. Sedimentation of homogeneous suspensions of non-Brownian spheres. Phys. Fluids 9 (3), 491–499.

Ladd, A.J.C., 2002. Effects of container walls on the velocity fluctuations of sedimenting spheres. Phys. Rev. Lett. 88 (4), 04830-1–04830-4.

Ladd, A.J.C., Verberg, R., 2001. Lattice-Boltzmann simulations of particle–fluid suspensions. J. Stat. Phys. 104 (5/6), 1191–1251.

Marchioro, M., Tanksley, M., Prosperetti, A., 2000. Flow of spatially non-uniform suspensions. Part I: Phenomenology. Int. J. Multiphase Flow 26, 783–831.

Marchioro, M., Tanksley, M., Wang, W., Prosperetti, A., 2001. Flow of spartially non-uniform suspensions. Part II: Systematic derivation of closure relations. Int. J. Multiphase Flow 27, 237–276.

Mo, G., Sangani, A., 1994. A method for computing Stokes-flow interactions among spherical objects and its application to suspensions of drops and porous particles. Phys. Fluids 6 (5), 1637–1652.

Rothman, D.H., Zaleski, S., 1997. Lattice-Gas Cellular Automata, first ed. Cambridge University Press.

Rowe, P.N., 1964. Volumetric method for calculating the flow around moving objects in lattice-Boltzmann schemes. Trans. Inst. Chem. Engrs. 42, T55.

Saffman, P.G., 1973. On the settling speed of free and fixed suspensions. Stud. Appl. Math. 52, 115–127.

Sangani, A.S., Acrivos, A., 1982. Slow flow through a periodic array of spheres. Int. J. Multiphase Flow 8 (4), 343–360.

Succi, S., 2001. The Lattice Boltzmann Equation for Fluid Dynamics and Beyond, first ed. Oxford University Press.

Sundaresan, S., 2003. Instabilities in fluidized beds. Ann. Rev. Fluid Mech. 35, 63–88.

Wang, W., Prosperetti, A., 2001. Flow of spatially non-uniform suspensions. Part III: closure relations for porous media and spinning particles. Int. J. Multiphase Flow 27 (9), 1627–1653.

Wylie, J.J., Koch, D.L., C, L.A.J., 2003. Rheology of suspensions with high particle inertia and moderate fluid inertia. J. Fluid Mech. 480, 95–118.

Zhang, D., Prosperetti, A., 1994. Averaged equations for inviscid disperse twophase flow. J. Fluid Mech. 5, 185–219.